Journal of Materials Chemistry A

Accepted Manuscript

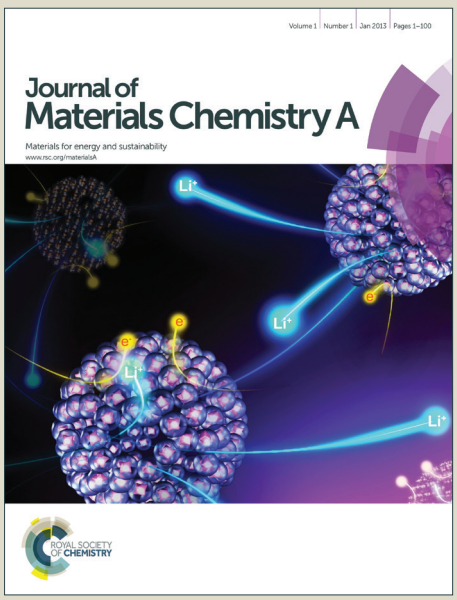

ROYAL SOCIETY OF CHEMISTRY

www.rsc.org/materialsA

Journal of Materials Chemistry A RSCPublishing

ARTICLE

Structural influence of porous FeO_x@C nanorods on their performance as anodes of lithium-ion battery

Cite this: DOI: 10.1039/x0xx00000x

Xueying Li,[a] Zhiyun Zhang,[a] Jing Li,[a] Yuanyuan Ma*[a,b] and Yongquan Qu*[a,b]

Received 00th January 2012,
Accepted 00th January 2012

DOI: 10.1039/x0xx00000x

www.rsc.org/

Two types of porous iron oxide nanorods, FeO_x synthesized by hydrothermal (FeO_x-HY) with large internal voids and porous shells and FeO_x synthesized by annealing (FeO_x-AN) with mesopores of ~ 4.0 nm, were obtained by hydrothermal or high temperature treatments of β-FeOOH nanorods, respectively. Their performance as anode materials in lithium ion battery (LIB) were evaluated and correlated with the specific features of the porous structures. FeO_x-HY with large internal voids and porous shell exhibited a better cyclability than FeO_x-AN. With the assistance of a carbon coating, the FeO_x-HY@C electrode exhibited a steadily increased specific capacity with the increase of cycles, a high specific capacity of ~1131 mA h g^{-1} at a current density of 100 mA g^{-1} after 50 cycles. In comparison, the FeO_x-AN@C electrode delivered a slightly decreased cycling performance in the specific capacity and a smaller specific capacity at each current density. The structural features of FeO_x-HY@C with the large internal voids, porous thin shells and the elastic carbon shell can effectively buffer volume swing and mechanical stresses, synchronize lithium diffusion and charge transport processes, and facilitate the lithium ion transport. These results suggest that the pore structure of the anode materials has a significant influence on their performance in LIBs.

1. Introduction

Iron oxide is one of the most promising anode materials for lithium ion batteries (LIBs) due to its accessibility, low processing cost, non-toxicity, and high theory capacity.[1] At the anode of LIBs occurs the reversible redox processes involving iron oxide and lithium that are accompanied with a significant volume change of iron oxide and subsequent loss of electrical contacts between the iron oxide and current collector.[2-4] As a result, compromised performances of LIBs, including large capacity fade, irreversibility, and poor life cycle, is commonly observed with the use of iron oxide.[5, 6] In principle, iron oxide with reduced particle size may endure a significant volume change without structural failure. However, electrodes fabricated from small particles of iron oxides tend to suffer from poor electrical conduction due to the existence of a large number of grain boundaries.[7] To solve this dilemma, strategies focusing on nano/micro hierarchical structures[3, 5] or hybrid structures with carbonaceous materials,[8, 9] which provide large surface areas for electrolyte contact and short path for lithium insertion/extraction, have been explored with the hopes of maintaining the material's structural integrity and improving its stability in lithium insertion/extraction cycles.

Differently structured iorn oxides, including hollow structures,[4, 10] mesoporous structures,[3, 11] nanoaggregates[12, 13] and carbon-incorporated iron oxide nanoparticles have been studied as anode materials of LIBs,[14, 15] amongst which porous iron oxides have been shown to display the best performance in terms of specific capacity, capacity retention, and rate capability.[16, 17]

The size and morphology of porous iron oxides can significantly affect their ability to accommodate the volume expansion. For example, the small pores cannot accept the expansive iron oxides, leading to the pulverization of the electroactive materials and the decayed cyclability as a sequence. Besides that porous nanostructures can buffer volume swing during the charge/discharge cycle, the structural features of porous iron oxides can greatly impact on the charge transfer, surface chemical reactions, chemical diffusion and cyclablity. Small pore size and large porous crystal size may not be favorable for chemical transfer within the electroactive iron oxides. Such structural features of porous iron oxides on their performance as electroactive materials for LIBs have not been studied.

Herein, two types of porous iron oxides with similar dimensions, iron oxide nanorods (FeO_x-HY) with large internal voids and porous shell and mesoporous iron oxide (FeO_x-AN) nanorods with a pore size of ~ 4.0 nm, were used as model structures to assess the effects of pore morphology on their electrical performance. FeO_x-HY nanorods were synthesized by hydrothermal treatment of β-FeOOH nanorods, while FeO_x-AN nanorods were obtained by calcinating β-FeOOH nanorods

at a high temperature. In the absence of a carbon shell, faded capacity was observed for both nanostructures. However, the FeO_x-HY exhibited a much better cyclability than the FeO_x-AN. The FeO_x-HY coated with a carbon shell delivered a higher specific capacity, a better rate capability, and a gradually increased capacity over cycling. In contrast, the FeO_x-AN with a carbon shell deliver a much smaller specific capacity. The better performance of FeO_x-HY@C is attributed to its larger internal voids, thinner porous shell and elastic carbon coating layer, all benefiting the electrical performance of iron oxides as the anodes of LIBs.

2. Experimental section

Ferric chloride ($FeCl_3 \cdot 6H_2O$) and urea were purchased from Sigma-Aldrich. All reagents are of analytical grade and used without further purification.

2.1 Synthesis of β-FeOOH nanorods

For a typical synthesis, 270 mg of $FeCl_3 \cdot 6H_2O$ and 120 mg of urea were mixed into 16 mL of deionized water under vigorous stirring. When the solution color changed into orange, the reaction solution was transferred into a 20 ml Teflon-lined stainless steel autoclave and maintained at 120 °C for 10 hrs. The brown products were collected by centrifugation and washed with copious amount of deionized water for several times.

2.2 Synthesis of FeO_x-HY nanorods by hydrothermal method

As-synthesized β-FeOOH nanorods (30 mg) were well dispersed in 10 mL of deionized water by ultrasonic treatment for 30 minutes. Hence, the aqueous solution was treated with the hydrothermal process at 180 ℃ for 12 h. Finally, the products were centrifuged off and washed with deionized water three times.

2.3 Synthesis of FeO_x-AN nanorods by high temperature annealing method

As-synthesized β-FeOOH nanorods (2.0 g) were loaded on a quartz boat and subjected to thermal treatment at 300 ℃ for 4 h. The ramping rate was controlled at 3 °C · min^{-1}.

2.4 Preparation of FeO_x@C porous nanorods

Porous iron oxides (50 mg) were dispersed in a solution containing 100 mg of glucose, 9 mL of deionized water, and 3 mL of ethanol. The mixture underwent hydrothermal treatment at 180 °C for 10 h. The products were centrifuged off, washed with ethanol and deionized water for five times alternatively, and dried at 100 °C overnight. The resulting product was treated at 450 °C with a ramping rate of 3 °C min^{-1} under Ar atmosphere and maintained at this temperature for 4 h.

2.5 Sample characterization

The samples were characterized by X-ray diffraction (XRD) (Smart Lab, Rigaku) using Cu Kα radiation, transmission electron microscopy (TEM, HT7700, Hitachi), and thermogravimetric analysis (TGA, TGA/DSC-1, Mettler Toledo). The surface area and pore size were measured by nitrogen physisorption (Micromeritics, ASAP 2020 HD88) based on the Brunauer-Emmet-Teller (BET) method. The specific surface area (S_{BET}) of the samples was calculated following the multipoint BET procedure. The pore-size distributions were determined using the Barrett-Joyner-Halenda (BJH) method.

2.6 Electrochemicl experiments

Electrochemical performances of the iron oxide porous nanorods were evaluated in Lithium cells (CR2032 coin type cell). The working electrodes were comprised of active materials, acetylene black, and polytetrafluoroethylene (PTFE) at a weight ratio of 8:1:1. Lithium metal was used as the counter electrode and the reference electrode. The electrolyte was 1M $LiPF_6$ dissolved in an ethylene carbonate (EC)/dimethyl carbonate (DMC)/diethyl carbonate (DEC) mixture (1:1:1, in wt%). Galvanostatic cycling experiments of the cells were performed on a LAND Ct2001A battery test system at the voltage window of 0.01-3.00 V versus Li^+/Li at room temperature. Cyclic voltammetry and impedance measurements of the electrodes was performed on the electrochemical workstation (Autolab)

3. Results and Discussion

3.1 Morphology comparison of FeO_x porous nanorods by different treatments

β-FeOOH nanorods were synthesized by a wet chemical process at 120 °C for 10 h.[18] TEM was used to examine the as-prepared β-FeOOH nanorods and FeO_x porous nanorods obtained by the hydrothermal treatment and the high temperature calcination on β-FeOOH nanorods. The TEM image of the β-FeOOH nanorods (Fig.1a) revealed the rod-like morphology with 40 ~ 50 nm in diameter and ~200 nm in length, consistent with previous reports.[19-21] XRD studies clearly indicate the major phase is tetragonal β-FeOOH (PDF Card No.34-1266) with small amount of α-Fe_2O_3 phase for as-synthesized nanorods (Fig. 1d).

It was found that hydrothermal treatments at 180 °C of the β-FeOOH nanorods induced a color change from dark brown to brick red. XRD results (Fig. 1d) confirmed that the hydrothermal treatments induced a phase transition from β-

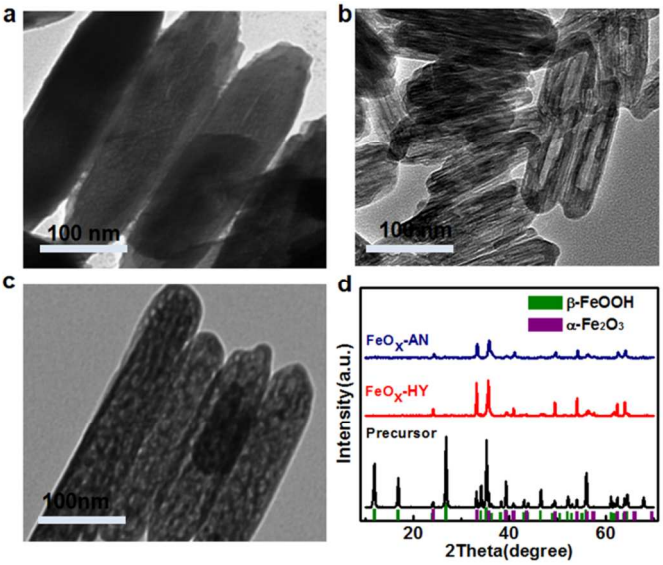

Fig. 1 TEM image and XRD pattern of β-FeOOH nanorods under hydrothermal treatment at different temperature.(a) β-FeOOH nanorods precursor;(b) the precursor treated at 180 °C for 12h by hydrothermal;(c) the precursor treated at 300 °C for 4h by annealing treatment;(d) the XRD pattern of β-FeOOH nanorods by hydrothermal and annealing treatment at different temperatures.

FeOOH phase into α-Fe_2O_3 phase. This phenomenon can be ascribed to the dehydration of β-FeOOH under the hydrothermal conditions. As shown in Fig.1b, the dehydrated nanostructures of α-Fe_2O_3 (FeO_x-HY) preserved the rod-like shape with the similar sizes of diameter and length, compared to those of β-FeOOH nanorods. Different from the previously reported porous iron oxides nanorods,[22-24] the TEM image in Fig. 1b reveals a novel porous structure with large internal voids and porous shells. The thickness of the shell is ~ 8 nm. Such structural features of Fe_2O_3-HY may benefit the electroactive materials as the anodes of LIBs. First of all, the large void within individual nanorods may afford the volume expansion during the redox reactions accompanied with the repeated Li^+ insertion/ extraction. Large voids and pores on the shells can facilitate electrolyte diffusion within the electrodes. The thickness of the shells is also beneficial to the redox reactions lithium ion insertion/extraction by providing a short pathway.[2, 4]

When the β-FeOOH nanorods were treated by high temperature annealing at 300°C, FeO_x-AN nanorods with pore sizes of 3 ~ 7 nm were achieved (Fig. 1c). This observation is consistent with previous studies.[22, 23] The XRD pattern of FeO_x-AN confirms the α-Fe_2O_3 phase of the nanorods.

Nitrogen gas adsorption/desorption isotherm measurements were used to determine surface area, average pore size, and pore volume of the porous iron oxides. Typical adsorption/desorption isotherms for FeO_x-HY and FeO_x-AN are shown in Fig. 2a and 2c. The standard multipoint BET analysis yields a surface area of 37.36 and 91.33 m^2 g^{-1} for FeO_x-HY and FeO_x-AN, respectively. The numerical difference can be attributed to the higher density of small pores in FeO_x-AN. As presented in Fig. 2b and 2d, the BJH analysis also indicates that the pore size of FeO_x-HY prepared by the hydrothermal approach is much larger than that treated by high temperature annealing method. As shown in Fig. 2b, the small fraction of

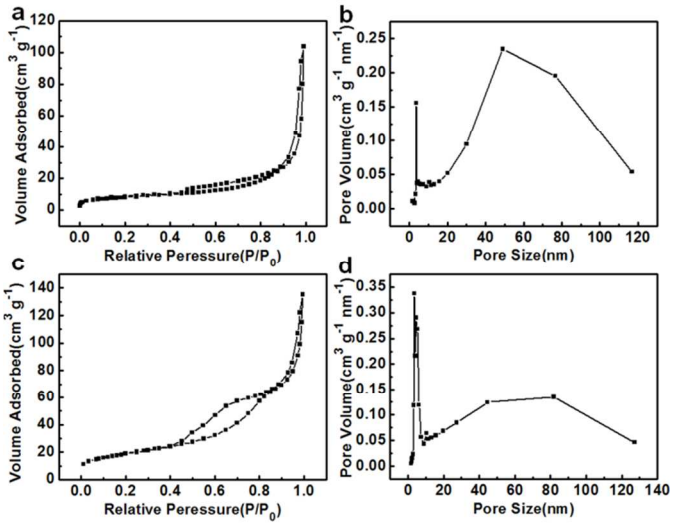

Fig. 2 (a) N_2 adsorption-desorption isotherms of FeO_x-HY; (b) Pore size distribution curves of FeO_x-HY; (c) N_2 adsorption-desorption isotherms of FeO_x-AN; (d) Pore size distribution curves of FeO_x-AN.

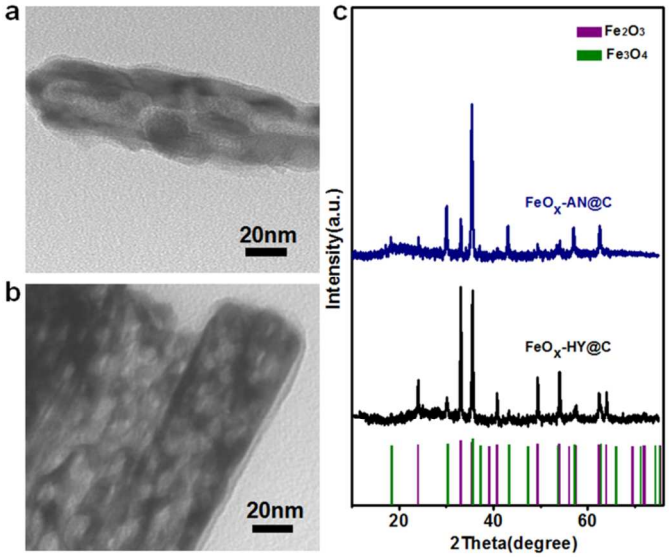

Fig. 3 TEM images and XRD patterns of FeO_x nanorods coated by carbon. (a) TEM image of FeO_x-HY coated by carbon (FeO_x-HY@C); (b) TEM image of FeO_x-AN coated by carbon (FeO_x-AN)@C); (c) XRD patterns of FeO_x-HY@C and FeO_x-AN@C. The green line represents PDF #19-0629 of Fe_3O_4, and the violet line represents PDF # 33-0664 of α-Fe_2O_3.

small pores was attributed to the nanopores on the shells of the FeO_x-HY, while the large pores observed from 20-120 nm can be ascribed to the hollow voids of the nanorods and packed pores. The results are consistent with the TEM observation in Fig. 2b, indicating the co-existence of two types of pores. In contrast, the mesoporous features of FeO_x-AN were reflected by their pore distribution, with the majority of pores ~ 4 nm.

3.2 Morphology comparison of FeO_x@C porous nanorods by different treatments

Integration of carbonaceous materials with iron oxides to form hybrid electroactive materials can not only effectively improve electrical conductivity of the electrodes but also significantly buffer the volume strain due to the elastic nature of carbon materials.[24-26] Hence, the electrical performance of iron oxides as anodes for LIBs can be greatly improved in the presence of incorporated carbon. Herein, nanorods integrated with a carbon shell were synthesized through carbonization of glucose by hydrothermal treatment followed by high temperature calcination under ambient conditions.

As shown in TEM images (Fig. 3), a carbon shell was successfully coated on the surface of FeO_x-HY and FeO_x-AN, denoted as FeO_x-HY@C (Fig. 3a) and FeO_x-AN@C (Fig. 3b), respectively. In Fig. 3a, the morphological features of FeO_x-HY were preserved with a carbon shell of ~ 2.0 nm. The carbon coated FeO_x-AN also preserved their initial porous structural features. A carbon shell thickness of ~2.0 nm was observed for FeO_x-AN@C (Fig.3b). The BET surface areas of FeO_x-HY@C and FeO_x-AN@C (Fig. S1, ESI†) were 31.33 and 80.47 m^2 g^{-1}, respectively. The surface areas of both FeO_x-HY@C and FeO_x-AN@C are slightly reduced compared with those of FeO_x-HY (37.36 m^2 g^{-1}) and FeO_x-AN (91.33 m^2 g^{-1}), which demonstrates their structure integrity during the carbon-

coating process. XRD patterns of carbon-coated iron oxide nanorods shown in Fig. 3c indicate a mixture of hematite and magnetite for both iron oxide nanorods after the carbonization, which can be attributed to partial reduction of hematite into magnetite by glucose during the formation of the outer carbon layers.[25, 27] Analyzed from XRD patterns, the iron oxide in FeO_x-HY@C was composed of 80% of hematite and 20% magnetite. For FeO_x-AN@C, 78% of hematite was converted into magnetite. The carbon contents in these two samples could be quantitatively determined by thermo-gravimetric analysis (TGA, Fig. S2). The observed weight losses for FeO_x-HY@C and FeO_x-AN@C were 10.23%, 9.80%, respectively. Considering the phase change of iron oxides, the carbon contents in these two samples were 10.9% (FeO_x-HY@C), 12.5% (FeO_x-AN@C), respectively.

3.3 Electrochemical performance comparison of FeO_x-HY and FeO_x-AN with and without carbon coating

The electrochemical performances of the two types of porous structures of iron oxides with and without carbon shells were systematically investigated by galvanostatic charge/discharge measurements at various current densities. Fig. 4 shows the first five consecutive CVs of the four electrodes between 0.01 and 3.0 V at a scan rate of 0.5 mV s^{-1}. Metallic lithium was used as both counter and reference electrodes. In the first cycle, all electrodes exhibited similar profiles in the CV cycle. The cathodic scan resulted in a sharp peak centered at 0.5 V due to the decomposition of $LiFeO_x$ and the crystal destruction accompanied by the complete reduction of Fe^{3+} to Fe^0. The anodic scan displayed a broad peak at 1.66 V, in the FeO_x-HY, which corresponds to the oxidation of Fe^0 to Fe^{3+} ions and reformation of FeO_x. The FeO_x-AN anodic peak is more positive (~1.85 V). The difference is due to the more difficult oxidation process in the FeO_x-AN.[28, 29]

However, a dramatic difference for the subsequent four consecutive cycles was observed during the subsequent cycles in the CV curve of FeO_x-HY and FeO_x-AN. For the FeO_x-HY electrode (Fig. 4a), the peak current decreased significantly, indicating the "re-formation" or "conditioning" of the electrode in the first few cycles, whereby the active material underwent structural rearrangement and led to poor electrical contact with the conducting carbon particles in the composite electrode.[2, 28, 30] For the following scans in the CV profiles of FeO_x-HY, the cathodic peak was shifted to ~0.45 V and became broader. The shift in the peak potentials indicates the destruction of the crystal structure. Similar broadened and shifted redox peaks were also noted with iron oxides and their solid solutions, such as $ZnFe_2O_4$ and $NiFe_2O_4$.[31, 32] Thus, the CV curves of FeO_x-HY were shown in Fig. 3a are consistent with the galvanostatic cycling behavior of iron-based electrodes reported in the references.[2, 12] In contrast, the peaks of four consecutive CV curves (Fig. 4b) after the first scan nearly overlapped for the FeO_x-HY@C electrode but were slightly smaller than those of the first cycle, suggesting a possible stabilized cyclability of FeO_x-HY@C as the anodes of LIBs. The position of anodic peak is shift to 1.85V, corresponding to the oxidation of Fe^0 to $Fe^{2+/3+}$, which due to FeO_x-HY@C is a mixture of hematite and magnetite.[1, 33] The barely changed CV curve of the FeO_x-HY@C electrode indicates the integrated structure and favorable charge conductivity of the electroactive materials during the charge/discharge process. The thin shell of hollow nanorods, combined with the elastic carbon shell, could effectively buffer the volume expansion. Carbon-coating facilitates the formation of a stable SEI film on the surface of the electrode material.[33, 34] The current densities and the positions of oxidation /reduction peaks are almost the same during the electrode redox reaction, indicating a good reversibility during the lithium ion insertion and extraction processes. The similar phenomena of the decreased redox current densities for FeO_x-AN and the stabilized current densities for FeO_x-AN@C were also observed as shown in Fig. 4c and 4d, respectively.

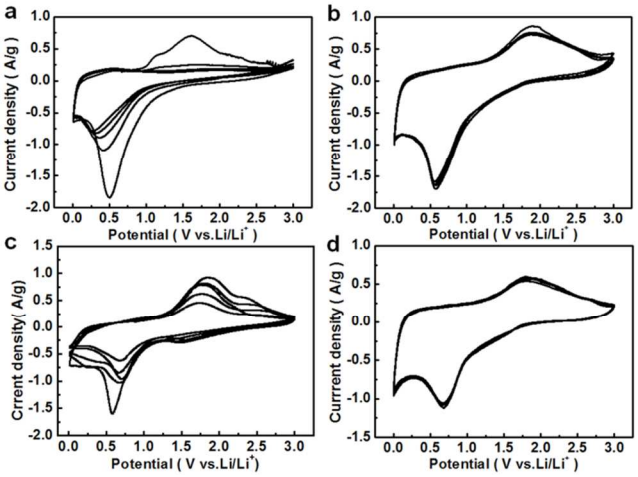

Fig. 4 Cyclic voltammetry profiles of the electroactive materials between 0.01 and 3.0V at a scan rate of 0.5 mV s^{-1}. (a) FeO_x-HY; (b) FeO_x-HY@C; (c) FeO_x-AN; and (d) FeO_x-AN@C.

The cycling performance of FeO_x-HY and FeO_x-AN electrodes were carried out under the current density of 0.1 A g^{-1}, as given in Fig. S3 (ESI†). The current density was calculated based on the mass of electroactive materials. The FeO_x-HY electrode showed an initial specific capacity of 781.1 mA h g^{-1} and maintained 30.9 % of the initial value after 30 cycles. The faded capacity is in agreement with the decreased current densities observed in the CV curves (Fig. 4a). FeO_x-AN showed a much higher specific capacity of 1105 mA h g^{-1} initially, but faded very quickly. After 30 cycles, a capacity retention of 7.4 % was observed. The better cycliability of FeO_x-HY, over FeO_x-AN, originates from the structural features of FeO_x-HY, in which the large internal voids and porous thin shell of the hollow nanorods can facilitate chemical diffusion within electrodes, providing a short pathway for lithium insertion/extraction and partially affording the volume expansion.

However, the completely stabilized electrochemical performance has not been realized due to the hollow porous nanorods, where 50% of the voids (calculated from the TEM images) cannot accommodate the volume swing during the charge/discharge process. Moreover, ~8 nm thickness of shell may not be thin enough to release the strain caused by volume expansion and maintain the structural integration. Hence, FeO_x-HY with a thin carbon shell as anodes for LIBs were also evaluated.

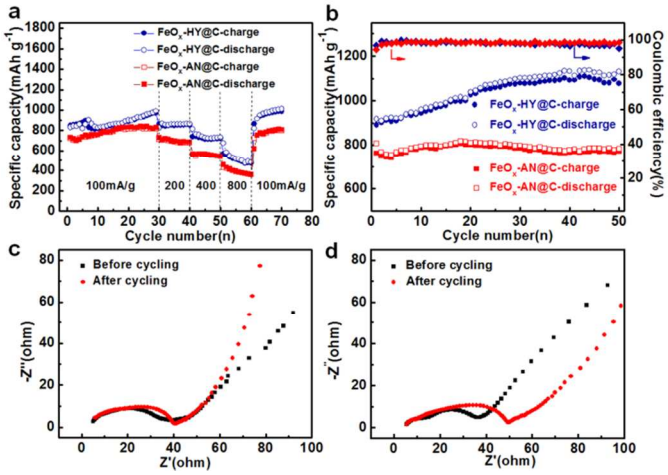

Fig. 5 (a) Discharge and charge capacity of the FeO_x-HY@C and FeO_x-AN@C electrodes at various current densities between a voltage window of 0.01-3 V. (b) Discharge and charge capacities versus cycle number of FeO_x-HY@C and FeO_x-AN@C at the current density of 0.1 A g^{-1}. The red plot represents the Coulombic efficiency of the FeO_x-AN@C electrode. The blue plot represents the Coulombic efficiency of the FeO_x-HY@C electrodes. (c) Nyquist plots of the FeO_x-HY@C electrodes before (black curve) and after (red curve) cycling. (d) Nyquist plots of the FeO_x-AN@C electrode before (black curve) and after (red curve) cycling.

Fig. 5a shows the rate performance of the FeO_x-HY@C and FeO_x-AN@C under different current densities with a cut-off window of 0.01~3.00 V. After 30 cycles, FeO_x-HY@C exhibited a specific capacity of 1056.2 mA h g^{-1} at 0.1 A g^{-1}. Increasing the current density to 0.2 A g^{-1} resulted in a reduced specific capacity of 922.3 mA h g^{-1}. At the high current densities of 0.4 and 0.8 A g^{-1}, the specific capacities decreased to 773.3 and 546.8 mA h g^{-1}, respectively. As the current density was restored to 0.1 A g^{-1}, the specific capacity of FeO_x-HY@C was 1066.2 mA h g^{-1}, which was even higher than the original value. The results indicate the FeO_x-HY@C electrode displays a good rate capability and can be reversibly cycled. Different to FeO_x-HY@C, the specific capacity of FeO_x-HY@C was relatively stable during the initial 5 cycles.

Subsequently, the specific capacity of FeO_x-AN@C starts to be increased. After 30 cycles, the specific capacity of FeO_x-AN@C got to 828.9 mA h g^{-1}. Changing the current density, the specific capacities were 695.64, 566.39, and 394.24 mAh g^{-1} at the current densities of 0.2, 0.4 and 0.8 A g^{-1}, respectively. When the current density was back to 0.1 A g^{-1}, the specific capacity of 800.28 mA h g^{-1} was close to the value at the 30th cycle. The specific capacity of FeO_x-HY@C was much larger than that of FeO_x-AN@C at the each current density. The results undoubtedly give the conclusion that the FeO_x-HY@C with large internal voids and a thin porous shell benefit their electrical performance as the active materials of anodes for LIBs. Notably, the different ratio of Fe_2O_3 and Fe_3O_4 in FeOx-HY@C and FeOx-AN@C cannot induce the obvious change in their specific capacities and their performance in cycliability of the two samples due to their close theory capacities of Fe_2O_3 (1007 mAh g^{-1}) and Fe_3O_4 (926 mAh g^{-1}) and large volume expansion during lithium insertion/extraction.

Fig. 5b shows the galvanostatic charge/discharge curves of the FeO_x-HY@C and FeO_x-AN@C electrodes at a rate of 0.1 A g^{-1} in the voltage range of 0.01~3.00 V. For the FeO_x-HY@C electrode, discharge and charge capacities of 918 and 891 mA h g^{-1} were delivered for the 1st lithium intercalation process. The initial Coulombic efficiency of 97.4% was related to the formation of a solid electrolyte interphase layer accompanying the electrolyte decomposition. The carbon-coated FeO_x-HY delivered gradually increased specific capacities as high as 1071 mA h g^{-1} at the 20th cycle. Such an activation process can be attributed to the reversible lithium storage in SEI layer, which was also observed in previous reports of iron oxide-based anodes of LIBs.[7, 8, 29] The specific capacity tended to be stabilized at 1131 mA h g^{-1} at the 50th cycle, which demonstrated a superior charge/discharge cycling stability of the FeO_x-HY@C as active materials for lithium ion storage. In contrast, the specific capacity of the FeO_x-AN@C electrode showed a continuous decrease after activation process during initial 20 cycles, from 811.47mAh g^{-1} at the 20th cycle to 783.6 mAh g^{-1} after 50 cycles, a small capacity fading of 96.6 %.

It is worthwhile to note that FeO_x-HY@C and FeO_x-AN@C have much different composition as shown in XRD spectra (Fig. 3c). Derived from their compositions and theoretical specific capacities of hematite and magnetite, the calculated theoretical capacities for iron oxides in FeO_x-HY@C and FeO_x-AN@C are 990.8 and 943.8 mAh g^{-1}, respectively. Both hematite and magnetite suffer from the volume swing during charge/discharge process. Hence, the different ratio of hematite and magnetite in FeO_x-HY@C and FeOx-AN@C cannot result in the large difference in their specific capacities and cycliability (Fig. 5a), which can be attributed to their different features of porous structures.

The morphology of FeO_x-HY@C and FeO_x-AN@C subjected to 50 charge/discharge cycles were characterized by TEM after dissolving SEI layer from their surface. As shown in Fig. 6a, the TEM image of FeO_x-HY@C after 50 cycles exhibited a similar morphology to the structure before cycling with the carbon-coating. Although the porous shell is pulverized, the internal voids and the integrated shell confined by the carbon shell preserved the structural stability of the FeO_x-HY@C. As shown in electron impedance spectroscopy (Fig. 5), the Nyquist plots of the FeO_x-HY@C electrode before and after cycling showed a semicircle in the high-frequency domain and a straight line in the low-frequency region, corresponding to the

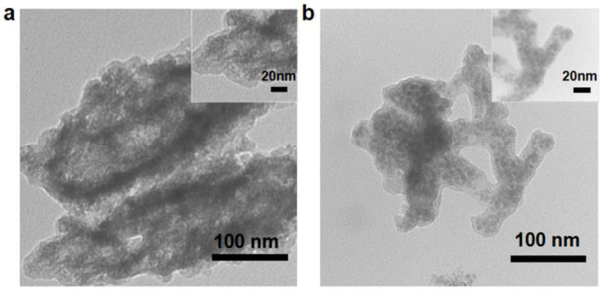

Fig. 6 TEM images of FeO_x@C after 50 cycles. (a) FeO_x-HY@C electrode and (b) FeO_x-AN@C electrode.

conductivity of the electrode and chemical transfer of lithium ions, respectively. After 50 cycles, the calculated resistance (40.2 Ω) of the FeO_x-HY@C electrode was nearly the same to that (39.0 Ω) before cycling (Fig. 5c), reflecting the structural integrity and good conductivity of the FeO_x-HY@C electrode. One semicircle before cycling changed into two nearly overlapped semicircles after 50 cycles, indicating that the process of lithium ion diffusion through the SEI layer almost synchronized with the process of the electron transport in the FeO_x-HY@C electrode.[35, 36] The straight line at the low frequency in the Nyquist polts represents the Warburg resistance related to the chemical transfer and electrolyte diffusion within the electrodes. The slope of the FeO_x-HY@C electrode increased from 57° for the initial cycle to 77° after 50 cycles, suggesting the improved lithium ion diffusion within the FeO_x-HY@C electrodes.

In contrast, the structure of FeO_x-AN@C was pulverized to smaller nanoparticles although a thin carbon shell was still observed (Fig. 6b). As shown in Fig. 5d, the calculated resistance (50.6 Ω) of the FeO_x-AN@C electrode after 50 cycles was larger than one (35.8 Ω) before cycling, indicating the decreased conductivity and subsequent muddle in lithium ion diffusion path induced by the pulverization. Thus, the lithium diffusion through the surface of SEI films and charge transport in the materials were slower than before cycling, as evidenced by a relatively large semicircle in high frequency range of Nyquist plots.[37, 38] The pulverized structure of the FeOx-AN@C after cycling cannot provide the largely available charge storage sites for rapid ionic pathways. The similar slopes of straight lines revealed that the lithium ion diffusion in the FeOx-AN@C electrode was not improved during the cycling. Compared to the Nyquist polts of the FeOx-HY@C electrode, the overall electroactive material utilization for the FeOx-AN@C electrode was reduced due to the asynchronous process of chemical diffusion and charge transfer. It can be employed to explain the small specific capacity of FeOx-AN@C. Hence, the preserved structural features of the hollow porous nanorods with the large internal voids and the thin porous shell still can greatly buffer the volume change during lithiation/delithiation and improve the chemical transfer and electrolyte diffusion. Moreover, the slope (~ 55.9°) of the FeOx-AN@C electrode was much smaller than that of the FeOx-HY@C electrode, indicating poor chemical transfer within the FeO_x-AN@C electrodes.

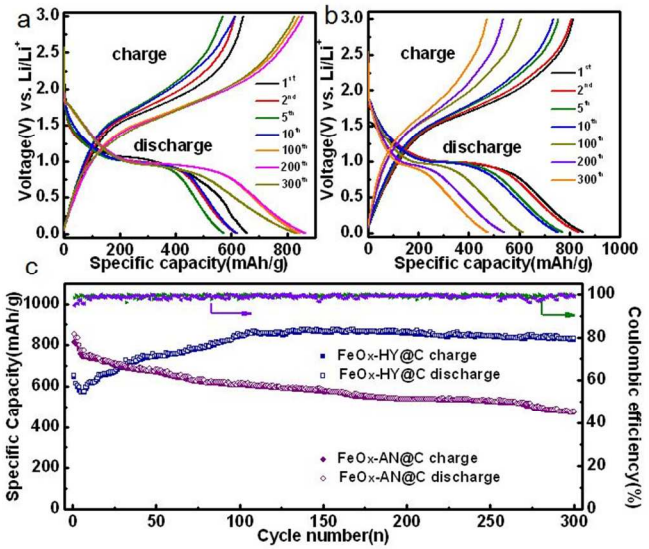

Fig. 7 Discharge-charge voltage profiles of FeO_x@C nanorods at different cycle numbers with the current density of 0.2 A g-1.(a) FeO_x-HY@C electrode and (b) FeO_x-AN@C electrode.(c) Discharge and charge capacities versus cycle number of FeO_x-HY@C and FeO_x-AN@C at the current density of 0.2 A g-1. The violet plot represents the Coulombic efficiency of the FeOx-AN@C electrode. The olive plot represents the Coulombic efficiency of the FeOx-HY@C electrodes.

The long-term cycling performance is expected for the anode materials of LIBs. The discharge-charge voltage profiles of FeO_x-HY@C and FeO_x-AN@C at 0.2 A g^{-1} are shown in Fig.7a and 7b, respectively. The potential plateau of FeO_x-HY@C in a range of 0.75-1.0V corresponds to the lithiation process while that in 1.5-2.0V to the delithiation process. In the 1st, 2nd and 5th cycles, discharge capacities of FeO_x-HY@C electrode are 655.9mAh g^{-1}, 616.7mAh g^{-1}, and 573mAh g^{-1}, respectively. The loss of capacity in the first few cycles is attributed to the formation of SEI films and decomposition of electrolyte. For the 10th, 100th, 200th and 300th cycles, the discharge capacities are 619.9 mAh g^{-1}, 846mAh g^{-1}, 865.3mAh g^{-1} and 832.2mAh g^{-1}, respectively. Moreover, the stable potential plateau of discharge profiles after 100 cycles indicates the superior and stable cycling of FeO_x-HY@C. The gradually increased capacity of FeO_x-HY@C can also be evidenced by the decreased voltage gap between charge and discharge profiles. Smaller voltage gap facilitate the reversible electrochemical reaction. The initial position of potential plateau in the discharge-charge curves of FeO_x-AN@C (Fig. 7b) is similar to that of FeO_x-HY@C (Fig. 7a). However, the polarization of FeO_x-AN@C is larger than the FeO_x-HY@C by cycling. The discharge capacities of the 1st, 2nd, 5th, 10th, 100th, 200th, 300th cycles are 855.2mAh g^{-1}, 837.7mAh g^{-1}, 773.8mAh g^{-1}, 753.7mAh g^{-1}, 614mAh g^{-1}, 540mAh g^{-1} and 475.8mAh g^{-1} with gradually shorten potential plateau of discharge curves. Meanwhile, the positions of potential plateau of charge curves shift to high voltage and lead to a large voltage gap between charge profiles and discharge profiles, with the increase of cycling. The results suggest the cycliability of FeO_x-AN@C is lower than that of FeO_x-HY@C.

Fig. 7c shows the long-term cycliability of FeO_x-HY@C and FeO_x-AN@C electrodes performed at the current density of 0.2A g^{-1} for 300 cycles. The capacity of the FeO_x-HY@C electrode is dramatically decreased after the initial cycles and then gradually increased. At the 200th, the capacity reached a stable value of 865.3 mA h g^{-1}. At the end of 300 cycles, the electrode delivered a capacity of 832.2 mAh g^{-1}, a 96.2% retention of that at the 100th cycle. In contrast, the continuously faded capacity of the FeO_x-AN@C electrodes with mesoporous structures is observed. After 300 cycles, the capacity of FeO_x-AN@C was remained at 475.8 mAh g^{-1}, which is only 55.6% of the initial cycle. Once again, the unique structure of FeO_x-HY@C, specifically the large internal voids and thin porous

shell, acts as the major contributions to the enhanced electrochemical kinetics and the stable cycling.

4. Conclusions

In conclusion, the pore structures of the electroactive materials can significantly influence their performance as the electrodes for LIBs. Herein, two types of porous iron oxide nanorods with similar dimensions, FeO_x-HY with large internal voids and thin porous shells and FeO_x-AN with mesopores of ~ 4.0 nm, were synthesized by the hydrothermal and high temperature annealing treatments on β-FeOOH nanorods, respectively. The FeO_x-HY coated with a carbon shell showed a large reversible capacity, a good rate capability, and an excellent cycling stability. In contrast, FeO_x-AN with carbon shell delivered a small specific capacity at each current density and a slightly faded capacity for cycling tests. Such differences can be attributed to the structural features of FeO_x-HY@C with the large voids, porous thin shell and the elastic carbon shell, which can effectively buffer volume swing and mechanical stresses during cycling process, synchronize lithium diffusion and charge transport processes, and facilitate the lithium ion transport.

Acknowledgements

We acknowledge the financial support from a NSFC Grant 21201138 and 21401148. This work was also partially funded by the Ministry of Science and Technology of China through a 973-program under Grant 2012CB619401 and by the Fundamental Research Funds for the Central Universities under Grant xjj2013102 and xjj2013043. Technical supports for TEM experiments from Frontier Institute of Science and Technology, Xi'an Jiaotong University, is also acknowledged.

Notes and references

[a] *Center of Applied Chemical Research, Frontier Institute of Science and Technology, and State Key Laboratory for Mechanical Behavior of Materials, Xi'an Jiaotong University, Xi'an, China 710049. E-mail: yongquan@mail.xjtu.edu.cn; yyma@mail.xjtu.edu.cn*

[b] *MOE Key Laboratory for Nonequilibrium Synthesis and Modulation of Condensed Matter, Xi'an Jiaotong University, Xi'an, 710049, China*

†Electronic Supplementary Information (ESI) available: [N_2 adsorption-desorption isotherms of FeO_x-HY@C and FeO_x-AN@C; pore size distribution curves of FeO_x-HY@C and FeO_x-AN@C. TGA curves of FeO_x-HY@C and FeO_x-AN@C. Discharge and charge capacities versus cycle number of FeO_x-HY and FeO_x-AN at the current density of 0.1 A g^{-1} between 0.01V and 3.0V.]. See DOI: 10.1039/c000000x/

1. C. T. Cherian, J. Sundaramurthy, M. Kalaivani, P. Ragupathy, P. S. Kumar, V. Thavasi, M. V. Reddy, C. H. Sow, S. G. Mhaisalkar, S. Ramakrishna and B. V. R. Chowdari, *J. Mater. Chem.*, 2012, **22**, 12198-12204.
2. J. Zhu, Z. Yin, D. Yang, T. Sun, H. Yu, H. E. Hoster, H. H. Hng, H. Zhang and Q. Yan, *Energy Environ. Sci.*, 2013, **6**, 987-993.
3. S. H. Lee, S. H. Yu, J. E. Lee, A. Jin, D. J. Lee, N. Lee, H. Jo, K. Shin, T. Y. Ahn, Y. W. Kim, H. Choe, Y. E. Sung and T. Hyeon, *Nano Lett.*, 2013, **13**, 4249-4256.
4. S. Xu, C. M. Hessel, H. Ren, R. Yu, Q. Jin, M. Yang, H. Zhao and D. Wang, *Energy Environ. Sci.*, 2014, **7**, 632-637.
5. J. S. Chen, T. Zhu, X. H. Yang, H. G. Yang and X. W. Lou, *J. Am. Chem. Soc.*, 2010, **132**, 13162-13164.
6. Z. Xiao, Y. Xia, Z. Ren, Z. Liu, G. Xu, C. Chao, X. Li, G. Shen and G. Han, *J. Mater. Chem.*, 2012, **22**, 20566-20573.
7. L. Zhang, H. B. Wu and X. W. Lou, *Adv. Energy Mater.*, 2014, **4**, 1300958.
8. W. Wei, S. Yang, H. Zhou, I. Lieberwirth, X. Feng and K. Müllen, *Adv.Mater.*, 2013, **25**, 2909-2914.
9. Q. An, F. Lv, Q. Liu, C. Han, K. Zhao, J. Sheng, Q. Wei, M. Yan and L. Mai, *Nano Lett.*, 2014, **14**, 6250-6256.
10. H. J. Kim, K. I. Choi, A. Pan, I. D. Kim, H. R. Kim, K. M. Kim, C. W. Na, G. Cao and J. H. Lee, *J. Mater. Chem.*, 2011, **21**, 6549-6555.
11. K. Brezesinski, J. Haetge, J. Wang, S. Mascotto, C. Reitz, A. Rein, S. H. Tolbert, J. Perlich, B. Dunn and T. Brezesinski, *Small*, 2011, **7**, 407-414.
12. J. Zhang, Y. Sun, Y. Yao, T. Huang and A. Yu, *J. Power Sources*, 2013, **222**, 59-65.
13. L. Zhang, H. B. Wu and X. W. Lou, *J. Am. Chem. Soc.*, 2013, **135**, 10664-10672.
14. J. Kan and Y. Wang, *Sci. Rep.*, 2013, **3**: 3502.
15. Q. Y. Hao, D. N. Lei, X. M. Yin, M. Zhang, S. Liu, Q. H. Li, L. B. Chen and T. H. Wang, *J. Solid State Electrochem.*, 2011, **15**, 2563-2569.
16. X. Xu, R. Cao, S. Jeong and J. Cho, *Nano Lett.*, 2012, **12**, 4988-4991.
17. B. Sun, J. Horvat, H. S. Kim, W.-S. Kim, J. Ahn and G. Wang, *J. Phys. Chem. C*, 2010, **114**, 18753-18761.
18. X. L. Fang, Y. Li, C. Chen, Q. Kuang, X. Z. Gao, Z. X. Xie, S. Y. Xie, R. B. Huang and L. S. Zheng, *Langmuir*, 2009, **26**, 2745-2750.
19. H. Maeda and Y. Maeda, *J. Chem. Phys.*, 2004, **121**, 12655-12665.
20. H. Maeda and Y. Maeda, *Phys. Rev. Lett.*, 2003, **90**, 18303-18307.
21. H. Maeda and Y. Maeda, *Langmuir*, 1996, **12**, 1446-1452.
22. P. Wu, N. Du, H. Zhang, J. Yu and D. Yang, *J. Phys. Chem. C*, 2011, **115**, 3612-3620.
23. S. M. Yuan, J. X. Li, L. T. Yang, L. W. Su, L. Liu and Z. Zhou, *Acs Appl. Mater. Interf.*, 2011, **3**, 705-709.
24. H. Geng, Q. Zhou, J. Zheng and H. Gu, *RSC Adv.*, 2014, **4**, 6430-6434.
25. P. Wang, M. X. Gao, H. G. Pan, J. L. Zhang, C. Liang, J. H. Wang, P. Zhou and Y. F. Liu, *J. Power Sources*, 2013, **239**, 466-474.
26. F. Cheng, J. Liang, Z. Tao and J. Chen, *Adv.Mater.*, 2011, **23**, 1695-1715.
27. W. M. Zhang, X. L. Wu, J. S. Hu, Y. G. Guo and L. J. Wan, *Adv. Funct. Mater.*, 2008, **18**, 3941-3946.
28. S. H. Lee, V. Sridhar, J. H. Jung, K. Karthikeyan, Y. S. Lee, R. Mukherjee, N. Koratkar and I. K. Oh, *ACS Nano*, 2013, **7**, 4242-4251.
29. X. Y. Li, L. Qin, Z. Y. Zhang, Z. Zhang, Y. Z. Zheng and Y. Q. Qu, *J. Mater. Chem. A*, 2015, **3**, 2158-2165.
30. Q. M. Zhang, Z. C. Shi, Y. F. Deng, J. Zheng, G. C. Liu and G. H. Chen, *J. Power Sources*, 2012, **197**, 305-309.
31. N. Wang, H. Xu, L. Chen, X. Gu, J. Yang and Y. Qian, *J. Power Sources*, 2014, **247**, 163-169.
32. Y. Xiao, J. Zai, X. Li, Y. Gong, B. Li, Q. Han and X. Qian, *Nano Energy*, 2014, **6**, 51-58.
33. L. W. Su, Y. R. Zhong and Z. Zhou, *J. Mater. Chem. A*, 2013, **1**, 15158-15166.
34. X. Gu, L. Chen, S. Liu, H. Xu, J. Yang and Y. Qian, *J. Mater. Chem. A*, 2014, **2**, 3439-3444.
35. P. G. Bruce and M. Y. Saidi, *Solid State Ionics*, 1992, **51**, 187-190.
36. M. Hirayama, H. Ido, K. Kim, W. Cho, K. Tamura, J. i. Mizuki and R. Kanno, *J. Am. Chem. Soc.*, 2010, **132**, 15268-15276.
37. A. K. Hjelm and G. Lindbergh, *Electrochim. Acta*, 2002, **47**, 1747-1759.
38. D. P. Abraham, S. Kawauchi and D. W. Dees, *Electrochim. Acta*, 2008, **53**, 2121-2129.